https://doi.org/10.5194/egusphere-2025-3367
Preprint. Discussion started: 6 August 2025

Constraining urban CO_2 emissions in Seoul using combined ground and satellite observations with Bayesian inverse modelling

Sojung Sim[1,2], Sujong Jeong[2]

[1]Environmental Planning Institute, Seoul National University, Seoul, 08826, Republic of Korea
[2]Climate Tech Center, Seoul National University, Seoul, 08826, Republic of Korea

Correspondence to: Sujong Jeong (sujong@snu.ac.kr)

Abstract. Accurate carbon emission estimates are essential for guiding climate action toward net zero emissions by 2050. The Bayesian inverse method, combined with atmospheric CO_2 measurements and the transport model, can serve as an independent verification approach to improve accuracy. In this study, we developed a Bayesian inverse modelling framework using ground- and space-based measurements and applied it to Seoul to test the framework and constrain its CO_2 emissions. By leveraging the high temporal resolution of ground-based in situ observations and the broad spatial coverage of satellite data, we improved the accuracy of emission estimates. Our results indicate a 4.43% increase in posterior emissions compared to prior estimates, suggesting that the prior emissions were slightly underestimated. The spatiotemporal variability of posterior emissions increased significantly, enabling us to track CO_2 fluctuations and assess the impact of carbon reduction policies over time and space. Additionally, the mean absolute error was reduced, improving the agreement between simulated and observed CO_2 enhancements. We thoroughly investigated the performance of the inverse model through a sensitivity analysis that considered different observational network configurations. The most substantial reductions in uncertainties (19.2%) were observed when all available observations were used. The extensive coverage of satellite observations enabled further corrections in areas not covered by ground observations. Overall, this study highlights the importance of combining multiple observational sources to better constrain urban CO_2 emissions. The framework also shows strong potential for application in other cities and can support the development of effective climate mitigation policies.

https://doi.org/10.5194/egusphere-2025-3367
Preprint. Discussion started: 6 August 2025

Graphical abstracts

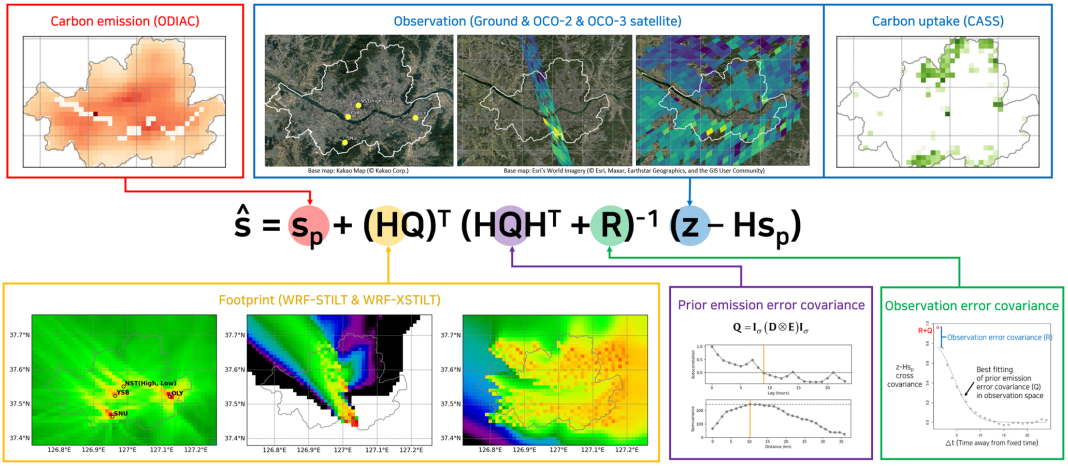

1 Introduction

Global carbon emissions from fossil fuel combustion and land-use change are redistributed among the atmosphere, ocean, and land (Friedlingstein et al., 2022). In the global carbon cycle, these five major components closely interact to maintain balance. However, anthropogenic emissions of greenhouse gases (GHGs), particularly carbon dioxide (CO_2), have dominated since the industrial era, resulting in rising atmospheric CO_2 levels and driving climate change (Friedlingstein et al., 2022). Human-caused climate change amplifies global surface temperatures and impacts weather extremes such as heatwaves, tropical cyclones, droughts, and heavy precipitation (IPCC, 2023). To mitigate the adverse effects of climate change worldwide, international climate agreements like the United Nations Framework Convention on Climate Change, the Kyoto Protocol, and the Paris Agreement have been implemented (IPCC, 2023). The IPCC 1.5℃ Special Report declared that achieving global net-zero CO_2 emissions by 2050 is imperative to limit the increase in global temperature to 1.5 ℃ above pre-industrial levels (IPCC, 2018). More than 130 countries have signalled an intention to reduce CO_2 emissions to near net-zero by around mid-century (Robinson and Shine, 2018).

By 2050, 68% of the world's population is projected to reside in urban areas (UN-DESA, 2018). At least 70% of global anthropogenic CO_2 emissions originate from cities (IEA, 2015). Given the concentration of population and CO_2 emissions in cities, they bear significant responsibility for emission reduction and are expected to play a major role in meeting their net-zero goals. The C40 Climate Leadership Group, comprising around 100 cities worldwide, has pledged to reduce GHG

https://doi.org/10.5194/egusphere-2025-3367
Preprint. Discussion started: 6 August 2025

emissions and developed a science-based approach (40 Cities, 2022). To support urban emission reduction strategies, the quality assurance of CO_2 emission estimates is required (Gurney et al., 2021; IPCC, 2019). Accurate emission estimates can provide detailed guidance to establish a baseline for prioritizing climate action and assessing policy progress over time (Mueller et al., 2021).

Various efforts are underway to estimate CO_2 emissions through a bottom-up approach. This approach calculates anthropogenic CO_2 emissions based on socio-economic databases (e.g., energy consumption, housing statistics, and road networks) and emission factors. Because of limited access to activity data and unknown emission factors within urban areas, detailed CO_2 emission estimates with high spatial and temporal resolution have been developed only for certain cities, such as Indianapolis (Gurney et al., 2012), Los Angeles (Feng et al., 2016; Gurney et al., 2019b), Salt Lake City (Patarasuk et al., 2016), and New York (Gately et al., 2015). Other types of emission data products, including CDIAC (Carbon Dioxide Information and Analysis Center), EDGAR (Emissions Database for Global Atmospheric Research), and ODIAC (Open-Data Inventory for Anthropogenic Carbon Dioxide), have been devised to downscale global/national total emission estimates using proxies such as nighttime lights and population. Large discrepancies between bottom-up and downscaled CO_2 emission estimates at the urban scale have been reported, primarily stemming from the large point sources and road traffic (Gurney et al., 2019a). Such uncertainties limit the establishment of a CO_2 emissions baseline and assessing mitigation outcomes at the city levels.

A complementary and independent approach to verify these CO_2 emission estimates is deemed necessary (IPCC, 2019). In the top-down approach, emission estimates can be constrained via real-time CO_2 measurements and atmospheric transport models. Consequently, combining bottom-up and top-down estimates has been explored using a Bayesian inversion approach for accurate CO_2 emission estimation. Bayesian inversion approach has been used in recent studies to optimize existing bottom-up estimates over Salt Lake City (Kunik et al., 2019; Mallia et al., 2020), Paris (Lian et al., 2022; Nalini et al., 2022), Los Angeles (Ye et al., 2020), and Tokyo (Ohyama et al., 2023; Pisso et al., 2019). They obtained optimal CO_2 emissions with the uncertainty reduction of 39.32% (Kunik et al., 2019), 27.7% (Mallia et al., 2020), 8–10% (Lian et al., 2022), 2–10% (Nalini et al., 2022), ~50% (Ohyama et al., 2023), and 20.09% (Pisso et al., 2019) compared to prior emissions.

Previous studies that performed inverse modelling for urban areas have primarily relied on a single type of observation to constrain emissions, most commonly ground-based in situ CO_2 measurements (Breón et al., 2015; Göckede et al., 2010; Lauvaux et al., 2016; Lian et al., 2023, 2022; Mallia et al., 2020; McKain et al., 2012; Nalini et al., 2022; Sargent et al., 2018; Staufer et al., 2016). Some studies have instead used ground-based Fourier Transform Infrared (FTIR) column-averaged CO_2 (XCO_2) observations (Hedelius et al., 2018; Ohyama et al., 2023), airborne observations (Lopez-Coto et al., 2020; Pitt et al., 2022), or satellite observations (Hamilton et al., 2024; Kaminski et al., 2022; Roten et al., 2023; Wu et al., 2018; Ye et al., 2020). However, studies that combine multiple observation types to leverage their complementary strengths remain rare. Although Pisso et al. (2019) integrated in situ airborne and ground-based observations to assess Lagrangian inverse modelling, and Che et al. (2024) combined ground-based FTIR and satellite data to estimate CO_2 emissions, these studies focused on either near-surface CO_2 concentrations or vertical CO_2 profiles, rather than incorporating both perspectives. In this study, we

https://doi.org/10.5194/egusphere-2025-3367
Preprint. Discussion started: 6 August 2025

integrate ground-based in situ CO_2 observations, which provide detailed information on surface emissions and uptake with high temporal resolution, and satellite observations, which offer broad spatial coverage and capture the total atmospheric CO_2 column. By combining these two complementary datasets, we simultaneously account for surface CO_2 fluxes and their impact on the vertical distribution of atmospheric CO_2. To our knowledge, this is the first inverse modelling study to fully utilize surface and column-integrated CO_2 measurements, providing a more comprehensive constraint on urban CO_2 emissions.

Seoul is a megacity with a population of approximately 10 million, which accounts for 18% of South Korea's total population in 2022 (KOSIS, 2023). The population and infrastructure in Seoul are densely concentrated, making it more susceptible to severe damage from climate change than other regions. It also has one of the highest carbon emissions among the 13,000 cities worldwide (Moran et al., 2018). Seoul has participated in the C40 Climate Leadership Group since 2006, and in 2020, it announced the '2050 GHGs Reduction Promotion Plan' to achieve a net-zero emissions goal (Seoul Metropolitan Government, 2021). Within Seoul, a comprehensive CO_2 monitoring network has been established, encompassing numerous stationary monitoring sites and mobile platforms to understand the urban carbon cycle (Park et al., 2020; Sim et al., 2020). Given its dense population, concentrated emissions, and extensive measurement networks, Seoul can be an optimal testbed city for studies to verify CO_2 emission estimates and assess the effectiveness of the CO_2 monitoring network.

In this study, we used a Bayesian inverse model and ground- and space-based measurements to improve the accuracy of CO_2 emission estimates over Seoul. We developed a high-resolution Bayesian inverse modelling framework with a spatial resolution of 0.01° and a temporal resolution of 1 h, incorporating anthropogenic CO_2 emissions, biogenic CO_2 fluxes, atmospheric CO_2 measurements, a Lagrangian transport model, and error covariances of both prior emissions and observations. We then estimated the optimal spatiotemporal distribution of CO_2 emissions over Seoul for December 2021, verifying existing emission data. Additionally, we evaluated the effectiveness of the inversion by comparing observed and simulated CO_2 enhancements using prior and posterior emissions. Finally, we conducted sensitivity tests on different observational datasets to assess their impact on emission estimates.

2 Data and methods

2.1 Bayesian inverse method

In this study, data assimilation is employed to estimate optimal (posterior) CO_2 emissions close to the true emissions. Data assimilation in CO_2 estimation optimally combines information from atmospheric CO_2 observations with a transport model and prior CO_2 emissions to produce accurate posterior estimates of CO_2 emissions. Posterior CO_2 emissions are derived through the minimization of the cost function (Enting, 2002; Tarantola, 1987) defined as follows:

$$\boldsymbol{L_s} = \frac{1}{2}(\boldsymbol{z} - \boldsymbol{H}\,\boldsymbol{s})^{\boldsymbol{T}}\boldsymbol{R}^{-1}(\boldsymbol{z} - \boldsymbol{H}\boldsymbol{s}) + \frac{1}{2}\left(\boldsymbol{s} - \boldsymbol{s_p}\right)^{\boldsymbol{T}}\boldsymbol{Q}^{-1}(\boldsymbol{s} - \boldsymbol{s_p}) \quad (1)$$

Where $\boldsymbol{z}$ is a vector of observed CO_2 enhancements, $\boldsymbol{H}$ is the Jacobian matrix of footprint values from the atmospheric transport model, $\boldsymbol{s}$ is a vector of the unknown true CO_2 emissions, $\boldsymbol{R}$ is the covariance of observational errors, $\boldsymbol{s_p}$ is a state vector of

https://doi.org/10.5194/egusphere-2025-3367
Preprint. Discussion started: 6 August 2025

prior CO_2 emissions, and **Q** is the covariance of prior emission errors. The solution obtained by minimizing the cost function defined in Eq. (1) yields the optimized posterior CO_2 emission estimates ($\hat{s}$), expressed as:

$$\hat{\boldsymbol{s}} = \boldsymbol{s_p} + (\boldsymbol{H}\,\boldsymbol{Q})^{\boldsymbol{T}}(\boldsymbol{H}\,\boldsymbol{Q}\boldsymbol{H}^{\boldsymbol{T}} + \boldsymbol{R})^{-\mathbf{1}}(\boldsymbol{z} - \boldsymbol{H}\boldsymbol{s_p}) \quad (2)$$

The posterior uncertainty covariance ($\boldsymbol{V_{\hat{s}}}$) can be expressed as:

$$\boldsymbol{V_{\hat{s}}} = \boldsymbol{Q} - (\boldsymbol{H}\,\boldsymbol{Q})^{\boldsymbol{T}}(\boldsymbol{H}\,\boldsymbol{Q}\boldsymbol{H}^{\boldsymbol{T}} + \boldsymbol{R})^{-\mathbf{1}}(\boldsymbol{H}\,\boldsymbol{Q}) \quad (3)$$

Using the posterior uncertainty covariance obtained from Eq. (3), the reduction in uncertainty resulting from the constraints on emissions can be calculated as:

$$\boldsymbol{Error\ \ reduction} = \frac{\sqrt{\boldsymbol{Q_{tot}}} - \sqrt{\boldsymbol{V_{\hat{s}\_tot}}}}{\sqrt{\boldsymbol{Q_{tot}}}} \times \mathbf{100}\,\% \quad (4)$$

Here, $\boldsymbol{Q_{tot}}$ represents the domain- and time-averaged covariance of prior emission errors and $\boldsymbol{V_{\hat{s}\_tot}}$ represents the domain- and time-averaged covariance of posterior emission errors.

In this study, we assessed the validity of posterior emissions resulting from the inverse model by calculating the reduced chi-squared value (χ_r^2) following Tarantola (1987). It is computed using the equation:

$$\chi_r^2 = \frac{1}{\nu}[(\mathbf{z} - \mathbf{H}\hat{\boldsymbol{s}})^{\boldsymbol{T}}\boldsymbol{R}^{-\mathbf{1}}(\boldsymbol{z} - \boldsymbol{H}\hat{\boldsymbol{s}}) + (\hat{\boldsymbol{s}} - \boldsymbol{s_p})^{\boldsymbol{T}}\boldsymbol{Q}^{-\mathbf{1}}(\hat{\boldsymbol{s}} - \boldsymbol{s_p})] \quad (5)$$

Where the squared data residual ($\mathbf{z} - \mathbf{H}\hat{\boldsymbol{s}}$) and emissions residual ($\hat{\boldsymbol{s}} - \boldsymbol{s_p}$) from the inversion are normalized by their respective variance matrices, $\boldsymbol{R}$ and **Q**. The residuals are expected to follow a chi-squared distribution with ν degrees of freedom, which in this study corresponds to the number of observations. The closer the reduced chi-squared value is to 1, the more accurately the prescribed errors of observations and prior emissions are set, leading to a more reliable estimation of posterior emissions.

2.2 Observations

A set of measurements from ground-based and satellite observations, all collected during December 2021, was selected to obtain atmospheric CO_2 concentrations in Seoul. Although ground-based observations offer the advantage of real-time measurements of atmospheric CO_2 concentrations over an extended period, satellite observations provide broader spatial coverage.

For the ground measurements, we used observed CO_2 concentrations from five different sites in Seoul (Park et al., 2020): Namsan Seoul Tower-High (NST_H), Namsan Seoul Tower-Low (NST_L), Olympic Park (OLP), Seoul National University (SNU), and Yongsan Building (YSB), as shown in Fig. 1. The instrument inlet heights of NST_H, NST_L, OLP, SNU, and YSB, combined with the site altitude, are 420, 265, 27, 173, and 113 m, respectively. The observation instruments installed at NST_L and OLP are PICARRO's G2301, whereas those installed at NST_H, SNU, and YSB are LICOR's LI-850. We utilized only daytime data (10:00–16:00 KST) for the inverse modelling to minimize the impact of model biases in the planetary boundary layer height. The CO_2 concentrations measured at each ground observation site exhibit different patterns of variation because of differences in altitudes and surrounding environments (Fig. 2a). The average daytime CO_2 concentrations at NST_H, NST_L,

https://doi.org/10.5194/egusphere-2025-3367
Preprint. Discussion started: 6 August 2025

OLP, SNU, and YSB were 453.7 ± 19.6, 460.1 ± 27.1, 460.2 ± 26.7, 461.5 ± 26.6, and 466.9 ± 31.4 ppm, respectively. The lowest average concentration at NST_H is attributed to its location at the top of the tall tower, whereas the highest average concentration at YSB is because of its location in a commercial area with high vehicle traffic.

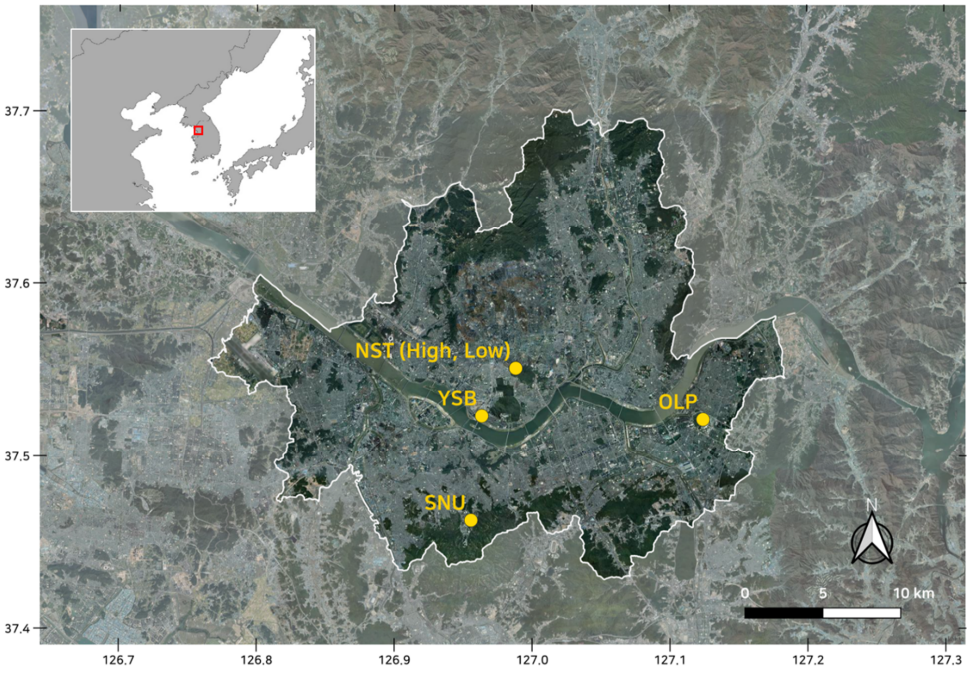

Figure 1: Map of Seoul with the locations of CO_2 ground observation sites: Namsan Tower-high (NST_H), Namsan Tower-low (NST_L), Olympic Park (OLP), Seoul National University (SNU), and Yongsan Building (YSB). Observation sites are denoted with yellow points. The background map is sourced from Kakao Map (© Kakao Corp.).

We used data from the Orbiting Carbon Observatory-2 (OCO-2) and the Orbiting Carbon Observatory-3 (OCO-3) for satellite measurements. OCO-2 and OCO-3, launched on July 2, 2014, and May 4, 2019, respectively, observe the dry-air column-averaged volume mixing ratio of CO_2 (XCO_2). On December 4 and 5, 2021, the OCO-2 and OCO-3 satellites passed over Seoul at 13:00 and 11:00 KST, respectively, yielding 60 and 167 soundings (Figs. 2b and 2c). Only good-quality data were considered when processing the XCO_2 data for observational input in inverse modelling. In both datasets, the XCO_2 values were higher in the southern part of Seoul compared to the northern part.

https://doi.org/10.5194/egusphere-2025-3367
Preprint. Discussion started: 6 August 2025

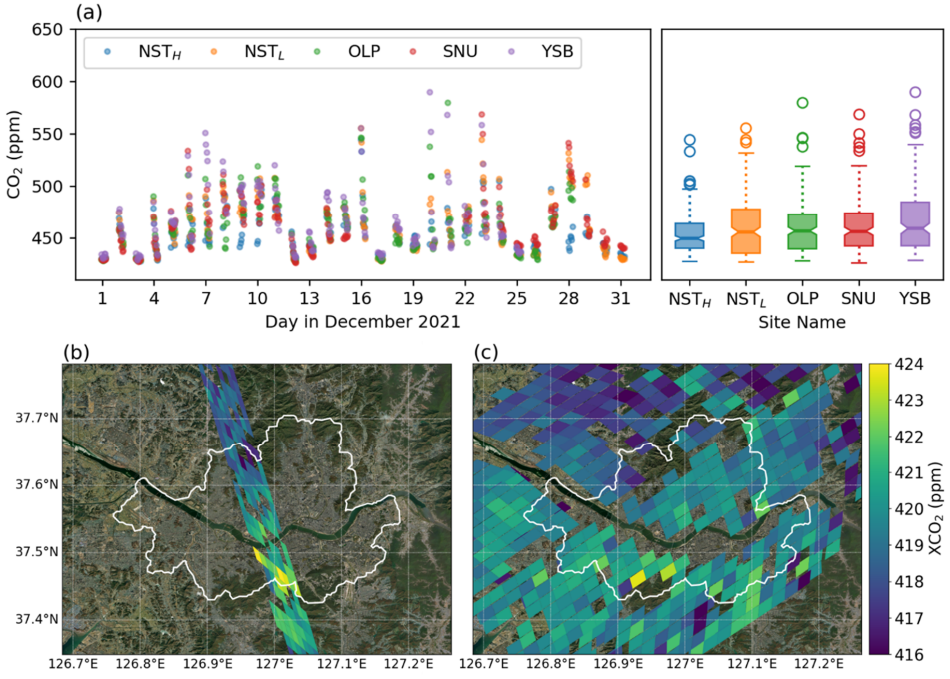

Figure 2: Observation data used in the Bayesian inverse modelling framework over Seoul during December 2021. (a) Time series of daytime-only (10:00–16:00 KST) CO_2 concentrations measured at five ground sites and box plot of the daytime CO_2 concentrations from ground sites. Spatial distributions of XCO_2 measured by (b) OCO-2 on December 4, 2021, at 13:00 KST and (c) OCO-3 on December 5, 2021, at 11:00 KST. The background maps in (b) and (c) are based on Esri's World Imagery (© Esri, Maxar, Earthstar Geographics, and the GIS User Community).

The vector of observed CO_2 enhancements, denoted as **z** in Eq. (1), represents the $\triangle CO_2$ affected by nearby emission sources. Because we aim to optimize Seoul's CO_2 emissions using atmospheric observations, we must calculate $\triangle CO_2$ influenced only by anthropogenic emissions within Seoul, excluding the effects of background and biogenic fluxes. To obtain the $\triangle CO_2$, the background and vegetation-affected concentrations must be subtracted from the observed CO_2 concentrations. We defined the background value for ground observations using the 24-h moving 5th percentile values from each site (Chandra et al., 2016; Gamage et al., 2020). For satellite observations, the background value was calculated from the daily median of measured XCO_2 over non-urban areas within a ~500,000 km^2 background box centered among Seoul (Labzovskii et al., 2019; Park et al., 2021). The calculation method for the vegetation-affected concentration is described in Sect. 2.4.

https://doi.org/10.5194/egusphere-2025-3367
Preprint. Discussion started: 6 August 2025

2.3 Atmospheric Transport

The Weather Research and Forecasting model with the (X-)Stochastic Time-Inverted Lagrangian Transport (WRF-(X)STILT) was used to derive the Jacobian matrix of footprint values (***H***) at a fine spatial resolution (e.g., 0.01°). We employed the STILT model (Fasoli et al., 2018; Lin et al., 2003) for ground-based observations and X-STILT (Wu et al., 2018) for satellite observations, both driven by meteorological fields from WRF model version 3.9.1 (Skamarock and Klemp, 2008). WRF-(X)STILT is an effective tool for simulating realistic atmospheric transport using a Lagrangian particle dispersion model within the planetary boundary layer (Nehrkorn et al., 2010). Previous studies have widely used WRF-(X)STILT as an atmospheric transport model for applying GHG inverse modelling in urban areas (Kunik et al., 2019; McKain et al., 2012; Ohyama et al., 2023; Sargent et al., 2018; Wu et al., 2018; Zhao et al., 2009).

The model releases backward 3D virtual air particle trajectories with stochastically turbulent dispersion from the observation location (receptor) to potential source regions that influence the receptor. It then counts the dispersed air particles (footprints) in each grid. Footprints quantify the sensitivity of the observation to upstream source regions. They can be regarded as the average contribution of the surface flux at the receptor, as they represent how densely and how long the air particles lingered backward in time within each discretized volume of the upwind source regions. In Bayesian inverse modelling, the footprint acts as an operator, connecting individual CO_2 observations (unit: ppm) and gridded fluxes (unit: μmol/(m^2 s)). Using footprints representing concentration per unit flux allows direct comparison between CO_2 emissions and atmospheric CO_2 enhancements. For WRF-STILT, one thousand air particles were released from each observation site and tracked backward in time for 24 h (Fig. 3a). In the case of WRF-XSTILT, one thousand air particles were released from each column level for OCO-2 and OCO-3 soundings and tracked backward for 24 h (Figs. 3b and 3c). The column receptors consisted of 37 levels at 100 vertical spacing up to 3000 m above ground level (a.g.l.) and 500 vertical spacing up to 6000 m a.g.l. thereafter. Details on the WRF configuration and footprint calculation for STILT and X-STILT are provided in Texts S1 and S2 of the supplementary material, respectively.

https://doi.org/10.5194/egusphere-2025-3367
Preprint. Discussion started: 6 August 2025

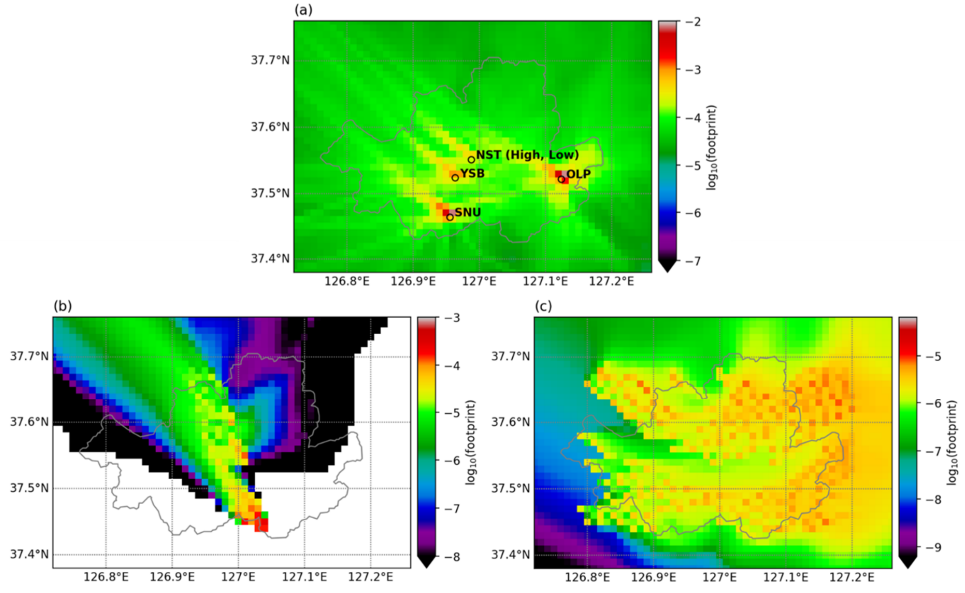

Figure 3: Footprint averages on a $\log_{10}$ scale to upwind source regions of (a) ground observations, (b) OCO-2 satellite data, and (c) OCO-3 satellite data across the Seoul domain. The footprints are calculated using only daytime observation (10:00–16:00 KST) for December 2021. The footprint units are ppm/(μmol/(m²·s)). Note that the footprint ranges differ in panels (a), (b), and (c) for visualization purposes.

2.4 CO_2 emissions & biogenic fluxes

2.4.1 Anthropogenic CO_2 emissions

We used anthropogenic CO_2 emissions data from ODIAC version 2022 as prior emissions (Oda et al., 2018; Oda and Maksyutov, 2011). ODIAC provides global fossil fuel CO_2 emission estimates at a high spatial resolution of 1 × 1 km², using power plant profiles and space-based nighttime light data (Oda et al., 2018). ODIAC is based on the CDIAC national emissions estimates, which categorize emissions by fuel type—liquid, gas, solid fuel, cement, gas flare, and international bunker. The ODIAC dataset has been widely used in various research areas, such as urban emission evaluation, monitoring network design experiments, and the inverse estimation of CO_2 emissions (Che et al., 2024; Crowell et al., 2019; Fasoli et al., 2018; Hedelius et al., 2018; Kunik et al., 2019; Lauvaux et al., 2016; Lian et al., 2023, 2022; Mallia et al., 2020; Ohyama et al., 2023; Sim et al., 2023; Wu et al., 2018; Ye et al., 2020).

ODIAC is based on downscaling bottom-up CO_2 emission estimates using spatial proxies. Global geolocation information and power plant magnitudes are sourced from the Carbon Monitoring and Action database. However, this database occasionally

https://doi.org/10.5194/egusphere-2025-3367
Preprint. Discussion started: 6 August 2025

misplaces point sources, necessitating manual correction (Kunik et al., 2019; Ohyama et al., 2023). For instance, the Korea Central Power Corporation in Seoul, located in the western part of the city, is inaccurately positioned in the ODIAC data. To correct this spatial discrepancy, we customized the ODIAC data, as shown in Fig. S3 of the supplementary material. We manually relocated the misaligned point source to match the power plant location. Additionally, for the grid cell with significantly high CO_2 emissions mistakenly identified as a point source, we replaced the emission value with the average of the surrounding eight grid cells.

Because the temporal resolution of ODIAC is monthly, it is necessary to refine the data to achieve hourly CO_2 emission estimates. We applied weekly and diurnal temporal scaling factors (Nassar et al., 2013) specific to Seoul to adjust the monthly ODIAC emission data, as shown in Fig. S4 in the supplementary material. The weekly scaling factors for Seoul remain consistent on weekdays, with values exceeding 1, but decrease over the weekends (Fig. S4a). The diurnal scaling factors exhibit typical daily emission patterns, increasing in the morning, peaking in the afternoon, and decreasing in the evening (Fig. S4b). Figure S4c shows the hourly CO_2 emissions time series after applying these temporal scaling factors. After spatial and temporal pre-processing, the daytime (1–7 UTC) emissions for December 2021 serve as the state vector for prior CO_2 emissions, denoted as '$\boldsymbol{s_p}$' (Fig. 4a).

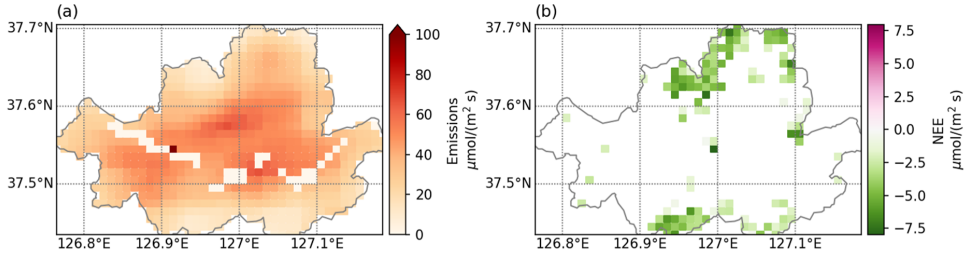

Figure 4: Averaged CO_2 fluxes of (a) prior emissions and (b) net biogenic ecosystem exchange over Seoul for daytime (10:00–16:00 KST) in December 2021.

2.4.2 Biogenic CO_2 fluxes

In the urban carbon cycle, atmospheric CO_2 is mainly influenced by emissions from fossil fuel combustion and vegetation carbon uptake. Given that Seoul has forests covering 25.3% of its total area (Korea Forest Service, 2021), the impact of biogenic CO_2 fluxes cannot be ignored. To account for the influence of biogenic CO_2 on the observed concentration, we incorporated biogenic CO_2 fluxes estimated by a data-based model known as CASS (Carbon Simulator from Space). CASS generates terrestrial carbon flux data from vegetation using information such as air temperature, relative humidity, photosynthetically active radiation, enhanced vegetation index, and land surface water index. CASS employs the random forest

https://doi.org/10.5194/egusphere-2025-3367
Preprint. Discussion started: 6 August 2025

method to determine optimal coefficients for each region and applies them to the estimation of carbon uptake. We utilized hourly net ecosystem exchange (NEE) data, which were resampled from a 250-meter resolution to 0.01°, as the biogenic CO_2 flux data within Seoul (Fig. 4b). CO_2 uptake can be observed in grids where Seoul's mountains and parks are located during the daytime. We obtained the vegetation-affected concentration by multiplying the footprints from the atmospheric transport model by the gridded biogenic CO_2 flux data using Eq. (S2) or (S4).

2.5 Prior error covariance

The prior error covariance matrix ($\boldsymbol{Q}$) is derived from both the variance in prior emissions uncertainty ($\boldsymbol{\sigma}$) and the temporal and spatial covariances ($\boldsymbol{D}$ and $\boldsymbol{E}$). We construct the prior error covariance matrix as follows:

$$\boldsymbol{Q} = \boldsymbol{I_\sigma}(\boldsymbol{D} \otimes \boldsymbol{E})\boldsymbol{I_\sigma} \tag{6}$$

Where $\boldsymbol{I_\sigma}$ is a diagonal matrix whose elements represent the uncertainty of prior emissions. Instead of directly constructing the full $\boldsymbol{Q}$ matrix, the temporal and spatial error covariance matrices are combined using a Kronecker product ($\otimes$) to reduce computational costs, particularly when dealing with large emission state vectors (Yadav and Michalak, 2013).

In previous studies on urban inverse modelling, three methods for estimating prior emissions uncertainty were mainly identified. Most studies assumed a relative uncertainty for prior estimates, such as 30% uncertainty for each emission source in Central California (Zhao et al., 2009), 15% for large point sources and 85% for the rest in Tokyo (Ohyama et al., 2023), 20% for Los Angeles and 40% for Riyadh and Cairo (Ye et al., 2020), 20% (Lian et al., 2022), and 60% (Nalini et al., 2022) for Paris. Kunik et al. (2019) and Mallia et al. (2020) defined the uncertainty of prior emissions as the difference between the prior and true emission estimates (e.g., Hestia). Another approach to estimating prior emissions uncertainty is inter-comparison with different inventories (Sargent et al., 2018; Wu et al., 2018). In this study, we assumed a relative uncertainty of 15% for large point sources and 100% for the rest of Seoul, similar to the approach used for Tokyo in Ohyama et al. (2023). For grids with prior emissions of 0 μmol m^{-2} s^{-1}, such as rivers, a minimum uncertainty value of 1 μmol m^{-2} s^{-1} was assigned, following the method of Kunik et al. (2019).

The temporal and spatial covariance matrices are defined using exponential decay equations:

$$\boldsymbol{D} = \exp\left(-\frac{\boldsymbol{X_\tau}}{\boldsymbol{l_\tau}}\right) \tag{7}$$

$$\boldsymbol{E} = \exp\left(-\frac{\boldsymbol{X_s}}{\boldsymbol{l_s}}\right) \tag{8}$$

The temporal covariance is computed based on lag-times ($\boldsymbol{X_\tau}$) between time steps, divided by temporal correlation range parameters ($\boldsymbol{l_\tau}$), where $\boldsymbol{l_\tau}$ represents the time at which errors in the prior emissions are considered uncorrelated. The spatial covariance is calculated using separation distances ($\boldsymbol{X_s}$) between grid cells, divided by spatial correlation range parameters ($\boldsymbol{l_s}$), where $\boldsymbol{l_s}$ indicates the distance at which errors in the prior emissions are considered uncorrelated. Previous studies have shown that suitable spatiotemporal correlation parameters vary by city. For example, in Salt Lake City, the temporal and spatial correlations were determined to be 2 d and 6 km, respectively (Kunik et al., 2019), whereas in Tokyo, the parameters were 0

https://doi.org/10.5194/egusphere-2025-3367
Preprint. Discussion started: 6 August 2025

d and 10 km (Ohyama et al., 2023). We performed a lagged autocorrelation function and variogram analysis to determine the optimal temporal and spatial correlation lengths for Seoul, respectively (Fig. S5). Based on the results, the optimal temporal and spatial correlation range parameters for the inversion over Seoul were 9 h and 10 km, respectively.

2.6 Observational error covariance

We estimated the observational error covariance ($\boldsymbol{R}$) using the departure-based diagnostics, commonly known as the Hollingsworth/Lönnberg method (Hollingsworth and Lönnberg, 1986; Lönnberg and Hollingsworth, 1986; Rutherford, 1972). The departure (or innovation) is defined as $\boldsymbol{z} - \boldsymbol{H}\boldsymbol{s}_{\boldsymbol{p}}$, representing the difference between the observed $\triangle CO_2$ and the values simulated by WRF-(X)STILT with prior emissions, following Eqs. (S2) and (S4). Because the standard deviation of departures reflects the combined effects of observation and prior emissions errors, we separate their contributions based on certain assumptions. The Hollingsworth/Lönnberg method assumes that prior emissions errors exhibit spatial correlation, whereas observation errors are spatially uncorrelated (Bormann et al., 2009). Additionally, prior emissions and observation errors are considered independent. Here, observation error includes uncertainties arising from the instrument, transport model, representation, background inflow (boundary conditions), and biogenic fluxes.

To estimate observation errors, we first compute the covariance of departure pairs as a function of separation distance. A function is then fitted to the covariance values at various distances, excluding the value at zero separation, and extrapolated to estimate the covariance at zero distance. At zero separation, the total variance is decomposed into a spatially correlated component (representing prior emissions error) and an uncorrelated component (representing observation error). Based on these assumptions, the value of the fit gives the prior emissions error in observation space at zero separation, and the observation error is determined by subtracting this value from the total covariance at zero distance.

In this study, we applied the Hollingsworth/Lönnberg method to estimate the observational error covariance for both ground-based and satellite observations. We first divided the observation vector into subsets: NST_H, NST_L, OLP, SNU, YSB, OCO-2, and OCO-3, assuming that error statistics within each subset are homogeneous. Because this method was originally developed for satellite data, which has wide spatial coverage but infrequent revisit cycles, we applied it directly for satellite observations. We assumed satellite observation errors are spatially uncorrelated and fitted a function (Limited-memory Broyden-Fletcher-Goldfarb-Shanno with Box constraints in R language) to the covariance as a function of separation distance. For ground-based observations, which provide data over a long period, we assumed that observation errors are temporally uncorrelated. Instead of using spatial distance, we fitted a function to the covariance as a function of time steps. The inferred observation error for each dataset was obtained by subtracting the value of the fit at zero separation (distance or time step) from the total covariance. The fitting results for each observation type are shown in Fig. S6. The inferred observation error was multiplied by the square of the standard deviation of departures, and the square of the mean departure was added to correct for bias. Finally, the estimated observation error for each observation was placed on the diagonal of the R matrix.

https://doi.org/10.5194/egusphere-2025-3367
Preprint. Discussion started: 6 August 2025

3 Results and discussion

In Sect. 3.1, we compare CO_2 emissions from prior and posterior estimates to investigate the spatiotemporal differences following the inversion run. In Sect. 3.2, we assess CO_2 enhancement between observations and simulations using prior and posterior emissions to evaluate the effectiveness of the inversion. Further exploration of sensitivity tests for observations using all data, only ground-based, only OCO-2, and only OCO-3 data, along with uncertainty reduction to estimate constraint effects, is presented in Sect. 3.3. A comprehensive discussion accompanies each set of results.

3.1 Comparison between prior and posterior emissions

We obtained posterior CO_2 emissions over Seoul for December 2021 using Bayesian inverse modelling, incorporating ground-based and satellite observations. Figure 5a compares the average CO_2 emissions between the prior and posterior estimates. The mean daytime prior and posterior emissions were 34.12 and 35.63 μmol m^{-2} s^{-1}, respectively. The average correction from prior to posterior emissions was approximately +4.43%, suggesting a slight increase in posterior emissions, and the prior emissions were slightly underestimated. However, the difference between the domain- and time-averaged prior and posterior emissions was not statistically significant. Similar findings have been reported in previous studies conducted in Tokyo (Ohyama et al., 2023). The reduced chi-squared value for the posterior emissions was 1.38. Although this is slightly higher than the ideal value of 1.0, it still indicates a reasonable representation of prior emissions error and observation error covariance assumptions. Further reducing this value closer to 1 would require assuming larger error metrics.

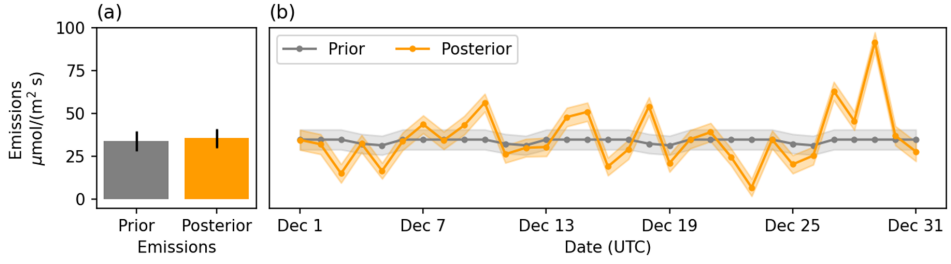

Figure 5: (a) Comparison of time- and domain-averaged emissions between prior and posterior estimates for December 2021 in Seoul, and (b) time series of domain-averaged daily (daytime average) prior and posterior CO_2 emissions, including emission uncertainties.

The daily time series of temporally resolved prior and posterior emissions averaged over the Seoul domain is shown in Fig. 5b. For prior emissions, the monthly ODIAC data was pre-processed using temporal scaling factors, resulting in higher emissions on weekdays and lower emissions on weekends. In contrast, posterior emissions exhibit greater temporal variability,

https://doi.org/10.5194/egusphere-2025-3367
Preprint. Discussion started: 6 August 2025

reflecting a more realistic pattern. Until December 22, posterior emissions fluctuated relative to prior emissions, but they showed a significant decrease on December 23, followed by a notable increase from December 27 to 29.

Figure 6 shows the spatial distribution of posterior CO_2 emissions and emission corrections from the inversion using all observation data over Seoul. Compared to the spatial patterns of prior CO_2 emissions in Fig. 4a, the posterior emissions in Fig. 6a exhibit a similar distribution, with higher emissions concentrated in central Seoul and lower emissions near the city's boundaries. However, the posterior correction map, obtained by subtracting prior emissions from posterior emissions, reveals spatial variations in emission adjustments ranging from −23.59 to 13.61 μmol m^{-2} s^{-1} (Fig. 6b). Most areas in Seoul experienced either increased or decreased emissions through Bayesian inverse modelling. Notably, emissions in the eastern part of Seoul were strongly corrected in the negative direction, whereas most other regions underwent positive corrections. This suggests that prior emissions were overestimated in the eastern part of Seoul and underestimated in the other areas.

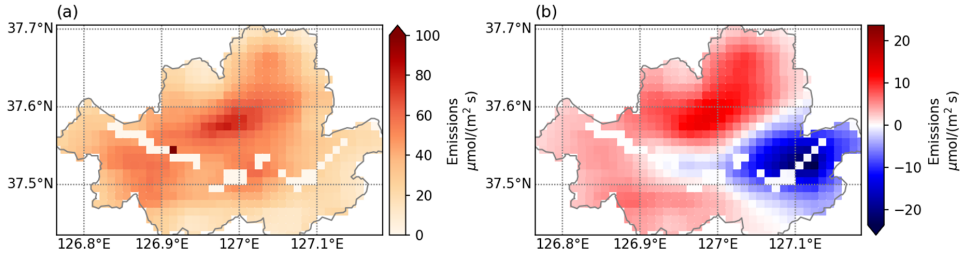

Figure 6: Averaged CO_2 fluxes over Seoul for daytime over December 2021. (a) Posterior emissions and (b) emission corrections (posterior minus prior) after the inversion run that used five ground sites, OCO-2, and OCO-3 data.

3.2 Comparison of CO_2 enhancement between observation and simulation

A comparison between observed CO_2 enhancements (OBS) and simulated CO_2 enhancements (MOD) was conducted to evaluate the performance of the inversion framework and assess how well atmospheric CO_2 data constrained emissions over Seoul. Figure 7 shows the changes in the relationship between OBS and MOD from prior to posterior emissions. MOD, based on prior emissions, was significantly lower than OBS, with a slope of 0.39 in Fig. 7a. However, after the inversion, the discrepancies were reduced, and MOD became closer to OBS, with the slope increasing to 0.71. Additionally, the correlation coefficient between OBS and MOD improved from 0.46 to 0.85, indicating a better agreement after the inversion. The mean absolute error between OBS and MOD also decreased significantly, from 12.18 to 6.64 ppm, when using posterior emissions data, shown in Fig. 7b. These results indicate that the inversion framework effectively constrained CO_2 emissions over Seoul by incorporating information from observational data.

https://doi.org/10.5194/egusphere-2025-3367
Preprint. Discussion started: 6 August 2025

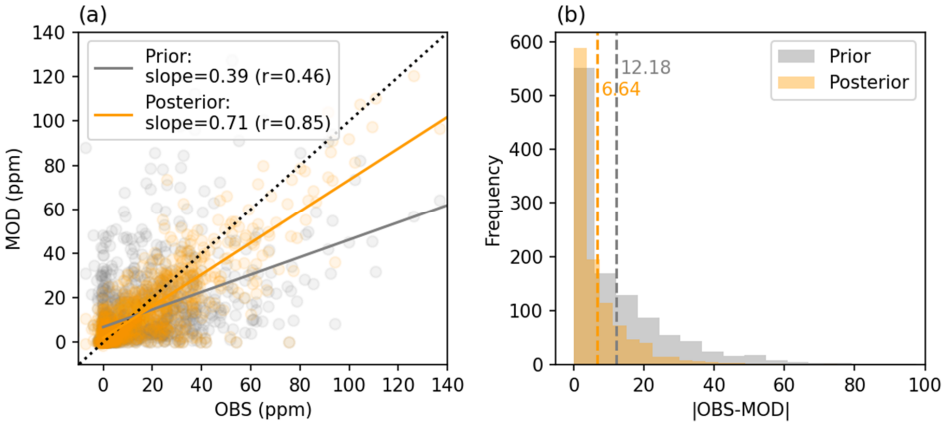

Figure 7: Comparison of observed CO_2 enhancements (OBS) and simulated CO_2 enhancements (MOD) using prior (gray) and posterior (orange) emissions during daytime over December 2021. (a) Scatter plots of OBS vs. MOD, with the slope and correlation coefficient (r). (b) Frequency distributions of absolute differences between OBS and MOD (|OBS-MOD|). The dashed lines in (b) indicate the mean absolute error between OBS and MOD.

3.3 Sensitivity test for observations used

We evaluated the performance of the inverse model through a sensitivity analysis considering different observational network configurations (Fig. 8). The cases included 1) using all observation data, 2) using only five ground sites, 3) using only OCO-2 data, and 4) using only OCO-3 data. The most substantial reductions in uncertainty were observed when all available observations were used, with an average reduction exceeding 19.2% (Fig. 8a). In this case, the spatial distribution of uncertainty reduction was similar to that obtained using only ground sites (Fig. 8b), as ground-based observations had a greater influence on the constraint than satellite data because of their continuous temporal coverage throughout the entire month. When using five ground sites, the uncertainty reduction in posterior emissions was 18.7%. The largest reductions occurred where ground observation sites were concentrated, particularly around OLP (eastern region), SNU (southern region), and surrounding NST_H, NST_L, and YSB. The reduction in uncertainty extended beyond the observation sites, covering the broader footprint influence range in Fig. 3a. Notably, a decrease was observed northwest of the observation sites, the upwind region. However, the impact on uncertainty reduction was minimal in western and northern Seoul, where no ground-based observation sites were present.

https://doi.org/10.5194/egusphere-2025-3367
Preprint. Discussion started: 6 August 2025

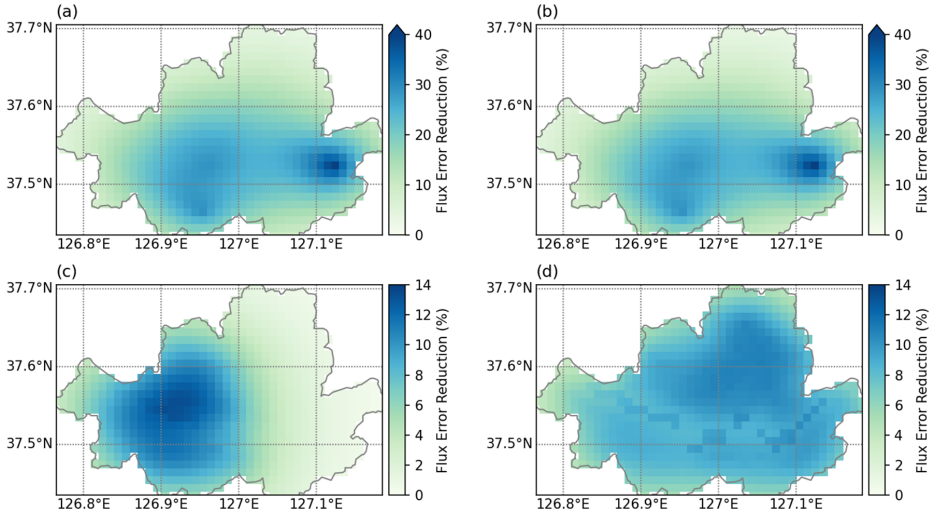

Figure 8: Daytime percent uncertainty reduction in posterior emissions over Seoul for the inverse analysis using different observation datasets: (a) all observation data from December 2021, (b) only five ground sites from December 2021, (b) only OCO-2 data from December 3–5, 2021, and (c) only OCO-3 data from December 3–5, 2021, when the satellite passed over Seoul. Note that the percent reduction ranges in panels (a), (b), (c), and (d) vary for visualization purposes.

Because OCO-2 and OCO-3 passed over Seoul on December 4 and 5, 2021, respectively, the uncertainty reduction results for satellite data are focused on December 3–5, highlighting the effect of satellite observations. The OCO-2 data significantly reduced the uncertainty of posterior emissions over western Seoul, with an average reduction of 6% (Fig. 8c). This can be attributed to the satellite's north-to-south overpass, covering the western footprint, an upwind region in Fig. 3b. OCO-2 contributed to uncertainty reduction in the western parts of Seoul, areas not covered by ground-based observations. Most of Seoul experienced uncertainty reduction due to OCO-3, which had 167 soundings across the city (Figure 8d). The domain-averaged uncertainty reduction from December 3–5 was 8.4%. OCO-3 contributed to uncertainty reduction in the northern region of Seoul, which was not covered by ground-based or OCO-2 observations. The extensive coverage of satellite observations enabled further corrections in areas lacking ground observations, demonstrating the added value of satellite constraints in reducing uncertainty.

https://doi.org/10.5194/egusphere-2025-3367
Preprint. Discussion started: 6 August 2025

4 Summary and conclusions

This study developed a Bayesian inverse modelling framework (version 1) to optimize CO_2 emissions using both ground- and space-based observations and applied it to Seoul. By incorporating high-resolution (0.01° spatial, 1 h temporal) anthropogenic and biogenic CO_2 fluxes, atmospheric CO_2 measurements, a Lagrangian transport model, and uncertainty quantification, we improved the accuracy of emission estimates. Ground-based (NST_H, NST_L, OLP, SNU, YSB) and satellite (OCO-2, OCO-3) observations from December 2021 were used to constrain emissions, with WRF-(X)STILT footprints linking emissions to observed CO_2 enhancements.

Although the averaged CO_2 emissions difference between prior and posterior estimates was relatively small (4.43% increase), the inversion revealed significant spatiotemporal variations. Posterior emissions exhibited greater variability, highlighting underestimation in most areas and overestimation in eastern Seoul. This information enables us to track when and where CO_2 emissions fluctuate and assess the impact of carbon reduction policies over time and space. Comparing observed and simulated CO_2 enhancements confirmed the effectiveness of the inversion, reducing the mean absolute error by nearly half. Sensitivity tests showed that ground- and space-based data achieved the greatest uncertainty reduction (19.2%), with OCO-2 and OCO-3 providing critical constraints in areas lacking ground-based observations. These results emphasize the complementary role of satellite data, particularly OCO-3's snapshot capability, in enhancing urban CO_2 monitoring.

Despite these improvements, some limitations remain, which future work will address. First, the inversion results depend on the accuracy of the transport model, introducing uncertainties in simulating atmospheric transport. Future improvements to WRF-(X)STILT will incorporate terrain elevation data that more closely represent real-world topography and implement observation nudging to enhance transport accuracy. Second, the analysis was limited to a 1-month, which may not fully capture seasonal emission variations. Extending the analysis to a full year will enable comparisons with Korea's national greenhouse gas inventory. Third, although the reduced chi-square value has been evaluated, additional validation using independent datasets such as radiocarbon ($\Delta^{14}C$) and flux tower measurements will be conducted. Finally, expanding the observational network will allow this approach to be applied to other cities and eventually to all of Korea, enabling a more comprehensive assessment of spatiotemporal CO_2 distribution, identifying regional emission hotspots, and improving the accuracy of national-scale carbon budget estimates to support mitigation policies.

By integrating high-resolution inverse modelling with multiple observational sources, this study provides a robust framework for quantifying urban CO_2 emissions. The findings refine emission estimates by reducing uncertainties and support data-driven policymaking for effective carbon mitigation strategies. Importantly, the proposed framework is designed to be transferable and applicable to other cities, contributing to broader efforts in long-term climate change mitigation.

https://doi.org/10.5194/egusphere-2025-3367
Preprint. Discussion started: 6 August 2025

Data Availability

The prior emissions data from ODIAC were obtained from the Center for Global Environmental Research (https://db.cger.nies.go.jp/dataset/ODIAC). Biogenic CO2 fluxes data from the CASS were downloaded from the Korea Carbon Project website (https://korea-carbon-project.org/map). The WRF model is freely distributed to the scientific community by the National Center for Atmospheric Research (NCAR) and can be accessed at https://www2.mmm.ucar.edu/wrf/users/download/get_source.html. The STILT and X-STILT models available for installation at https://uataq.github.io/stilt/#/ and https://github.com/uataq/X-STILT, respectively. OCO-2 and OCO-3 satellite data are publicly available from https://ocov2.jpl.nasa.gov/science/oco-2-data-center/ and https://ocov3.jpl.nasa.gov/science/oco-3-data-center/, respectively.

Competing interests

The authors declare that they have no conflict of interest.

Acknowledgments

This work was supported by Korea Environmental Industry & Technology Institute (KEITI) through "Project for developing an observation-based GHG emissions geospatial information map", funded by Korea Ministry of Environment (MOE) (RS-2023-00232066).

References

40 Cities: C40 Annual Report 2022, Miner. Commod. Ltd ACN 008 478 653, 134, 2022.

Bormann, N. (ECMWF R. D. ., Collard, A. (ECMWF R. D. ., and Bauer, P. (ECMWF R. D. .: Estimates of spatial and inter-channel observation error characteristics for current sounder radiances, ECMWF Tech. Memo., 1–41, 2009.

Breón, F. M., Broquet, G., Puygrenier, V., Chevallier, F., Xueref-Remy, I., Ramonet, M., Dieudonné, E., Lopez, M., Schmidt, M., Perrussel, O., and Ciais, P.: An attempt at estimating Paris area CO2 emissions from atmospheric concentration measurements, Atmos. Chem. Phys., 15, 1707–1724, https://doi.org/10.5194/acp-15-1707-2015, 2015.

Chandra, N., Lal, S., Venkataramani, S., Patra, P. K., and Sheel, V.: Temporal variations of atmospheric CO2 and CO at Ahmedabad in western India, Atmos. Chem. Phys., 16, 6153–6173, https://doi.org/10.5194/acp-16-6153-2016, 2016.

Che, K., Lauvaux, T., Taquet, N., Stremme, W., Xu, Y., Alberti, C., Lopez, M., García-Reynoso, A., Ciais, P., Liu, Y., Ramonet, M., and Grutter, M.: CO2 Emissions Estimate From Mexico City Using Ground- and Space-Based Remote Sensing, JGR Atmos., 129, 2024.

https://doi.org/10.5194/egusphere-2025-3367
Preprint. Discussion started: 6 August 2025

Crowell, S., Baker, D., Schuh, A., Basu, S., Jacobson, A. R., Chevallier, F., Liu, J., Deng, F., Feng, L., McKain, K., Chatterjee, A., Miller, J. B., Stephens, B. B., Eldering, A., Crisp, D., Schimel, D., Nassar, R., O'Dell, C. W., Oda, T., Sweeney, C., Palmer, P. I., and Jones, D. B. A.: The 2015–2016 carbon cycle as seen from OCO-2 and the global in situ network, Atmos. Chem. Phys., 19, 9797–9831, https://doi.org/10.5194/acp-19-9797-2019, 2019.

Enting, I. G.: Inverse Problems in Atmospheric Constituent Transport, Cambridge University Press, 2002.

Fasoli, B., Lin, J. C., Bowling, D. R., Mitchell, L., and Mendoza, D.: Simulating atmospheric tracer concentrations for spatially distributed receptors: Updates to the Stochastic Time-Inverted Lagrangian Transport model's R interface (STILT-R version 2), Geosci. Model Dev., 11, 2813–2824, https://doi.org/10.5194/gmd-11-2813-2018, 2018.

Feng, S., Lauvaux, T., Newman, S., Rao, P., Ahmadov, R., Deng, A., Díaz-Isaac, L. I., Duren, R. M., Fischer, M. L., Gerbig, C., Gurney, K. R., Huang, J., Jeong, S., Li, Z., Miller, C. E., O'Keeffe, D., Patarasuk, R., Sander, S. P., Song, Y., Wong, K. W., and Yung, Y. L.: Los Angeles megacity: A high-resolution land-atmosphere modelling system for urban CO2 emissions, https://doi.org/10.5194/acp-16-9019-2016, 2016.

Friedlingstein, P., O'sullivan, M., Jones, M. W., Andrew, R. M., Gregor, L., Hauck, J., Le Quéré, C., Luijkx, I. T., Olsen, A., Peters, G. P., Peters, W., Pongratz, J., Schwingshackl, C., Sitch, S., Canadell, J. G., Ciais, P., Jackson, R. B., Alin, S. R., Alkama, R., Arneth, A., Arora, V. K., Bates, N. R., Becker, M., Bellouin, N., Bittig, H. C., Bopp, L., Chevallier, F., Chini, L. P., Cronin, M., Evans, W., Falk, S., Feely, R. A., Gasser, T., Gehlen, M., Gkritzalis, T., Gloege, L., Grassi, G., Gruber, N., Gürses, Ö., Harris, I., Hefner, M., Houghton, R. A., Hurtt, G. C., Iida, Y., Ilyina, T., Jain, A. K., Jersild, A., Kadono, K., Kato, E., Kennedy, D., Klein Goldewijk, K., Knauer, J., Korsbakken, J. I., Landschützer, P., Lefèvre, N., Lindsay, K., Liu, J., Liu, Z., Marland, G., Mayot, N., Mcgrath, M. J., Metzl, N., Monacci, N. M., Munro, D. R., Nakaoka, S. I., Niwa, Y., O'brien, K., Ono, T., Palmer, P. I., Pan, N., Pierrot, D., Pocock, K., Poulter, B., Resplandy, L., Robertson, E., Rödenbeck, C., Rodriguez, C., Rosan, T. M., Schwinger, J., Séférian, R., Shutler, J. D., Skjelvan, I., Steinhoff, T., Sun, Q., Sutton, A. J., Sweeney, C., Takao, S., Tanhua, T., Tans, P. P., Tian, X., Tian, H., Tilbrook, B., Tsujino, H., Tubiello, F., Van Der Werf, G. R., Walker, A. P., Wanninkhof, R., Whitehead, C., Willstrand Wranne, A., et al.: Global Carbon Budget 2022, Earth Syst. Sci. Data, 14, 4811–4900, https://doi.org/10.5194/essd-14-4811-2022, 2022.

Gamage, L. P., Hix, E. G., and Gichuhi, W. K.: Ground-Based Atmospheric Measurements of CO:CO2 Ratios in Eastern Highland Rim Using a CO Tracer Technique, ACS Earth Sp. Chem., 4, 558–571, https://doi.org/10.1021/acsearthspacechem.9b00322, 2020.

Gately, C. K., Hutyra, L. R., and Wing, I. S.: Cities, traffic, and CO2: A multidecadal assessment of trends, drivers, and scaling relationships, Proc. Natl. Acad. Sci. U. S. A., 112, 4999–5004, https://doi.org/10.1073/pnas.1421723112, 2015.

Göckede, M., Turner, D. P., Michalak, A. M., Vickers, D., and Law, B. E.: Sensitivity of a subregional scale atmospheric inverse CO2 modeling framework to boundary conditions, J. Geophys. Res. Atmos., 115, 2010.

Gurney, K. R., Razlivanov, I., Song, Y., Zhou, Y., Benes, B., and Abdul-Massih, M.: Quantification of fossil fuel CO2 emissions on the building/street scale for a large U.S. City, Environ. Sci. Technol., 46, 12194–12202, https://doi.org/10.1021/es3011282, 2012.

https://doi.org/10.5194/egusphere-2025-3367
Preprint. Discussion started: 6 August 2025

Gurney, K. R., Liang, J., O'Keeffe, D., Patarasuk, R., Hutchins, M., Huang, J., Rao, P., and Song, Y.: Comparison of Global Downscaled Versus Bottom-Up Fossil Fuel CO2 Emissions at the Urban Scale in Four U.S. Urban Areas, J. Geophys. Res. Atmos., 124, 2823–2840, https://doi.org/10.1029/2018JD028859, 2019a.

Gurney, K. R., Patarasuk, R., Liang, J., Song, Y., O'keeffe, D., Rao, P., Whetstone, J. R., Duren, R. M., Eldering, A., and Miller, C.: The Hestia fossil fuel CO2 emissions data product for the Los Angeles megacity (Hestia-LA), Earth Syst. Sci. Data, 11, 1309–1335, https://doi.org/10.5194/essd-11-1309-2019, 2019b.

Gurney, K. R., Liang, J., Roest, G., Song, Y., Mueller, K., and Lauvaux, T.: Under-reporting of greenhouse gas emissions in U.S. cities, Nat. Commun., 12, 1–7, https://doi.org/10.1038/s41467-020-20871-0, 2021.

Hamilton, S. D., Wu, D., Johnson, M. S., Turner, A. J., Fischer, M. L., Dadheech, N., and Jeong, S.: Estimating Carbon Dioxide Emissions in Two California Cities Using Bayesian Inversion and Satellite Measurements, Geophys. Res. Lett., 51, https://doi.org/10.1029/2024GL111150, 2024.

Hedelius, J. K., Liu, J., Oda, T., Maksyutov, S., Roehl, C. M., Iraci, L. T., Podolske, J. R., Hillyard, P. W., Liang, J., Gurney, K. R., Wunch, D., and Wennberg, P. O.: Southern California megacity CO2, CH4, and CO flux estimates using ground-and space-based remote sensing and a Lagrangian model, Atmos. Chem. Phys., 18, 16271–16291, https://doi.org/10.5194/acp-18-16271-2018, 2018.

Hollingsworth, A. and Lönnberg, P.: The statistical structure of short-range forecast errors as determined from radiosonde data. Part I: The wind field, Tellus A, 38A, 111–136, https://doi.org/10.1111/j.1600-0870.1986.tb00461.x, 1986.

IEA: Energy and Climate Change, World Energy Outlook Spec. Rep., https://doi.org/10.1038/479267b, 2015.

IPCC: GLOBAL WARMING OF 1.5 ° C an IPCC special report on the impacts of global, Ipcc, 2018.

IPCC: Global Warming of 1.5°C : Summary for Policymakers, Technical Summary and Frequently Asked Questions, 2019.

IPCC: Synthesis report of the IPCC sixth assessment report (AR6) Longer report, Eur. Univ. Inst., 2023.

Kaminski, T., Scholze, M., Rayner, P., Houweling, S., Voßbeck, M., Silver, J., Lama, S., Buchwitz, M., Reuter, M., Knorr, W., Chen, H. W., Kuhlmann, G., Brunner, D., Dellaert, S., Denier van der Gon, H., Super, I., Löscher, A., and Meijer, Y.: Assessing the Impact of Atmospheric CO2 and NO2 Measurements From Space on Estimating City-Scale Fossil Fuel CO2 Emissions in a Data Assimilation System, Front. Remote Sens., 3, 1–21, https://doi.org/10.3389/frsen.2022.887456, 2022.

Korea Forest Service: Statistical Yearbook of Forestry, 2021.

Korean Statistical Information Service: http://kosis.kr/.

Kunik, L., Mallia, D. V., Gurney, K. R., Mendoza, D. L., Oda, T., and Lin, J. C.: Bayesian inverse estimation of urban CO2 emissions: Results from a synthetic data simulation over Salt Lake City, UT, Elem. Sci. Anthr., 7, 1–16, https://doi.org/10.1525/elementa.375, 2019.

Labzovskii, L. D., Jeong, S.-J., and Parazoo, N. C.: Working towards confident spaceborne monitoring of carbon emissions from cities using Orbiting Carbon Observatory-2, Remote Sens. Environ., 233, 111359, https://doi.org/10.1016/j.rse.2019.111359, 2019.

https://doi.org/10.5194/egusphere-2025-3367
Preprint. Discussion started: 6 August 2025

Lauvaux, T., Miles, N. L., Deng, A., Richardson, S. J., Cambaliza, M. O., Davis, K. J., Gaudet, B., Gurney, K. R., Huang, J., O'Keefe, D., Song, Y., Karion, A., Oda, T., Patarasuk, R., Razlivanov, I., Sarmiento, D., and Wu, K.: High-resolution atmospheric inversion of urban CO2 emissions during the dormant season of the Indianapolis Flux Experiment (INFLUX), JGR Atmos., 121, 5091–6129, 2016.

Lian, J., Lauvaux, T., Utard, H., Bréon, F. M., Broquet, G., Ramonet, M., Laurent, O., Albarus, I., Cucchi, K., and Ciais, P.: Assessing the Effectiveness of an Urban CO2 Monitoring Network over the Paris Region through the COVID-19 Lockdown Natural Experiment, Environ. Sci. Technol., 56, 2153–2162, https://doi.org/10.1021/acs.est.1c04973, 2022.

Lian, J., Lauvaux, T., Utard, H., Bréon, F. M., Broquet, G., Ramonet, M., Laurent, O., Albarus, I., Chariot, M., Kotthaus, S., Haeffelin, M., Sanchez, O., Perrussel, O., Denier Van Der Gon, H. A., Dellaert, S. N. C., and Ciais, P.: Can we use atmospheric CO2 measurements to verify emission trends reported by cities? Lessons from a 6-year atmospheric inversion over Paris, Atmos. Chem. Phys., 23, 8823–8835, https://doi.org/10.5194/acp-23-8823-2023, 2023.

Lin, J. C., Gerbig, C., Wofsy, S. C., Andrews, A. E., Daube, B. C., Davis, K. J., and Grainger, C. A.: A near-field tool for simulating the upstream influence of atmospheric observations: The Stochastic Time-Inverted Lagrangian Transport (STILT) model, J. Geophys. Res. Atmos., 108, https://doi.org/https://doi.org/10.1029/2002JD003161, 2003.

Lönnberg, P. and Hollingsworth, A.: The statistical structure of short-range forecast errors as determined from radiosonde data. Part II: The covariance of height and wind errors, Tellus A, 38A, 137–161, https://doi.org/10.1111/j.1600-0870.1986.tb00461.x, 1986.

Lopez-Coto, I., Ren, X., Salmon, O. E., Karion, A., Shepson, P. B., Dickerson, R. R., Stein, A., Prasad, K., and Whetstone, J. R.: Wintertime CO2, CH4, and CO Emissions Estimation for the Washington, DC–Baltimore Metropolitan Area Using an Inverse Modeling Technique, Environ. Sci. Technol., 54, 2606–2614, 2020.

Mallia, D. V., Mitchell, L. E., Kunik, L., Fasoli, B., Bares, R., Gurney, K. R., Mendoza, D. L., and Lin, J. C.: Constraining Urban CO2 Emissions Using Mobile Observations from a Light Rail Public Transit Platform, Environ. Sci. Technol., 54, 15613–15621, https://doi.org/10.1021/acs.est.0c04388, 2020.

McKain, K., Wofsy, S. C., Nehrkorn, T., Eluszkiewicz, J., Ehleringer, J. R., and Stephens, B. B.: Assessment of ground-based atmospheric observations for verification of greenhouse gas emissions from an urban region, Proc. Natl. Acad. Sci., 109, 8423–8428, https://doi.org/10.1073/pnas.1116645109, 2012.

Moran, D., Kanemoto, K., Jiborn, M., Wood, R., Többen, J., and Seto, K. C.: Carbon footprints of 13 000 cities, Environ. Res. Lett., 13, 064041, 2018.

Mueller, K. L., Lauvaux, T., Gurney, K. R., Roest, G., Ghosh, S., Gourdji, S. M., Karion, A., DeCola, P., and Whetstone, J.: An emerging GHG estimation approach can help cities achieve their climate and sustainability goals, Environ. Res. Lett., 16, https://doi.org/10.1088/1748-9326/ac0f25, 2021.

Nalini, K., Lauvaux, T., Abdallah, C., Lian, J., Ciais, P., Utard, H., Laurent, O., and Ramonet, M.: High-Resolution Lagrangian Inverse Modeling of CO2 Emissions Over the Paris Region During the First 2020 Lockdown Period, J. Geophys. Res. Atmos., 127, 1–26, https://doi.org/10.1029/2021JD036032, 2022.

https://doi.org/10.5194/egusphere-2025-3367
Preprint. Discussion started: 6 August 2025

Nassar, R., Napier-Linton, L., Gurney, K. R., Andres, R. J., Oda, T., Vogel, F. R., and Deng, F.: Improving the temporal and spatial distribution of co2 emissions from global fossil fuel emission data sets, J. Geophys. Res. Atmos., 118, 917–933, https://doi.org/10.1029/2012JD018196, 2013.

Nehrkorn, T., Eluszkiewicz, J., Wofsy, S. C., Lin, J. C., Gerbig, C., Longo, M., and Freitas, S.: Coupled weather research and forecasting-stochastic time-inverted lagrangian transport (WRF-STILT) model, https://doi.org/10.1007/s00703-010-0068-x, 2010.

Oda, T. and Maksyutov, S.: A very high-resolution (1km×1 km) global fossil fuel CO2 emission inventory derived using a point source database and satellite observations of nighttime lights, Atmos. Chem. Phys., 11, 543–556, https://doi.org/10.5194/acp-11-543-2011, 2011.

Oda, T., Maksyutov, S., and Andres, R. J.: The Open-source Data Inventory for Anthropogenic CO2, version 2016 (ODIAC2016): a global monthly fossil fuel CO2 gridded emissions data product for tracer transport simulations and surface flux inversions, Earth Syst. Sci. Data, 10, 87–107, https://doi.org/10.5194/essd-10-87-2018, 2018.

Ohyama, H., Frey, M. M., Morino, I., Shiomi, K., Nishihashi, M., Miyauchi, T., Yamada, H., Saito, M., Wakasa, M., Blumenstock, T., and Hase, F.: Anthropogenic CO2 emission estimates in the Tokyo Metropolitan Area from ground-based CO2 column observations, EGUsphere, 2023, 1–38, https://doi.org/10.5194/egusphere-2023-256, 2023.

Park, C., Jeong, S., Park, H., Woo, J.-H., Sim, S., Kim, J., Son, J., Park, H., Shin, Y., Shin, J.-H., Kwon, S.-M., and Lee, W.-Y.: Challenges in Monitoring Atmospheric CO2 Concentrations in Seoul Using Low-Cost Sensors, Asia-Pacific J. Atmos. Sci., https://doi.org/10.1007/s13143-020-00213-2, 2020.

Park, H., Jeong, S., Park, H., Labzovskii, L. D., and Bowman, K. W.: An assessment of emission characteristics of Northern Hemisphere cities using spaceborne observations of CO2, CO, and NO2, Remote Sens. Environ., 254, 112246, https://doi.org/10.1016/j.rse.2020.112246, 2021.

Patarasuk, R., Gurney, K. R., O'Keeffe, D., Song, Y., Huang, J., Rao, P., Buchert, M., Lin, J. C., Mendoza, D., and Ehleringer, J. R.: Urban high-resolution fossil fuel CO2 emissions quantification and exploration of emission drivers for potential policy applications, Urban Ecosyst., 19, 1013–1039, https://doi.org/10.1007/s11252-016-0553-1, 2016.

Pisso, I., Patra, P., Takigawa, M., Machida, T., Matsueda, H., and Sawa, Y.: Assessing Lagrangian inverse modelling of urban anthropogenic CO2 fluxes using in situ aircraft and ground-based measurements in the Tokyo area, Carbon Balance Manag., 14, 1–23, https://doi.org/10.1186/s13021-019-0118-8, 2019.

Pitt, J. R., Lopez-Coto, I., Hajny, K. D., Tomlin, J., Kaeser, R., Jayarathne, T., Stirm, B. H., Floerchinger, C. R., Loughner, C. P., Gately, C. K., Hutyra, L. R., Gurney, K. R., Roest, G. S., Liang, J., Gourdji, S., Karion, A., Whetstone, J. R., and Shepson, P. B.: New York City greenhouse gas emissions estimated with inverse modeling of aircraft measurements, Elementa, 10, 1–13, https://doi.org/10.1525/elementa.2021.00082, 2022.

Robinson, M. and Shine, T.: Achieving a climate justice pathway to 1.5 °c, Nat. Clim. Chang., 8, 564–569, https://doi.org/10.1038/s41558-018-0189-7, 2018.

https://doi.org/10.5194/egusphere-2025-3367
Preprint. Discussion started: 6 August 2025

Roten, D., Lin, J. C., Das, S., and Kort, E. A.: Constraining Sector-Specific CO2 Fluxes Using Space-Based XCO2 Observations Over the Los Angeles Basin, Geophys. Res. Lett., 50, 1–11, https://doi.org/10.1029/2023GL104376, 2023.

Rutherford, I. D.: Data Assimilation by Statistical Interpolation of Forecast Error Fields, J. Atmos. Sci., 29, 809–815, 1972.

Sargent, M., Barrera, Y., Nehrkorn, T., Hutyra, L. R., Gately, C. K., Jones, T., Mckain, K., Sweeney, C., Hegarty, J., Hardiman, B., Wang, J. A., and Wofsy, S. C.: Correction: Anthropogenic and biogenic CO2 fluxes in the Boston urban region (Proceedings of the National Academy of Sciences of the United States of America (2018) 115 (7491-7496) DOI: 10.1073/pnas.1803715115), Proc. Natl. Acad. Sci. U. S. A., 115, E9507, https://doi.org/10.1073/pnas.1815348115, 2018.

Seoul Metropolitan Government: 2050 Seoul Climate Action Plan, 2021.

Sim, S., Jeong, S., Park, H., Park, C., Kwak, K. H., Lee, S. B., Kim, C. H., Lee, S., Chang, J. S., Kang, H., and Woo, J. H.: Co-benefit potential of urban CO2 and air quality monitoring: A study on the first mobile campaign and building monitoring experiments in Seoul during the winter, Atmos. Pollut. Res., 11, 1963–1970, https://doi.org/10.1016/j.apr.2020.08.009, 2020.

Sim, S., Jeong, S., Park, C., Shin, J., Kim, I., Ban, S., and Lim, C.-S.: Designing an Atmospheric Monitoring Network to Verify National CO2 Emissions, Asia-Pacific J. Atmos. Sci., https://doi.org/10.1007/s13143-023-00343-3, 2023.

Skamarock, W. C. and Klemp, J. B.: A time-split nonhydrostatic atmospheric model for weather research and forecasting applications, J. Comput. Phys., 227, 3465–3485, https://doi.org/10.1016/j.jcp.2007.01.037, 2008.

Staufer, J., Broquet, G., Bréon, F. M., Puygrenier, V., Chevallier, F., Xueref-Rémy, I., Dieudonné, E., Lopez, M., Schmidt, M., Ramonet, M., Perrussel, O., Lac, C., Wu, L., and Ciais, P.: The first 1-year-long estimate of the Paris region fossil fuel CO2 emissions based on atmospheric inversion, Atmos. Chem. Phys., 16, 14703–14726, https://doi.org/10.5194/acp-16-14703-2016, 2016.

Tarantola, A.: Inverse Problem Theory Methods for Data Fitting and Model Parameter Estimation, Elsevier Science, 644 pp., 1987.

UN-DESA: World Urbanization Prospects, 197–236 pp., 2018.

Wu, D., Lin, J. C., Fasoli, B., Oda, T., Ye, X., Lauvaux, T., Yang, E. G., and Kort, E. A.: A Lagrangian approach towards extracting signals of urban CO2 emissions from satellite observations of atmospheric column CO2 (XCO2): X-St, Geosci. Model Dev., 11, 4843–4871, 2018.

Yadav, V. and Michalak, A. M.: Improving computational efficiency in large linear inverse problems: an example from carbon dioxide flux estimation, Geosci. Model Dev., 6, 583–590, https://doi.org/10.5194/gmd-6-583-2013, 2013.

Ye, X., Lauvaux, T., Kort, E. A., Oda, T., Feng, S., Lin, J. C., Yang, E. G., and Wu, D.: Constraining Fossil Fuel CO2 Emissions From Urban Area Using OCO-2 Observations of Total Column CO2, J. Geophys. Res. Atmos., 125, e2019JD030528, https://doi.org/https://doi.org/10.1029/2019JD030528, 2020.

Zhao, C., Andrews, A. E., Bianco, L., Eluszkiewicz, J., Hirsch, A., MacDonald, C., Nehrkorn, T., and Fischer, M. L.: Atmospheric inverse estimates of methane emissions from Central California, J. Geophys. Res. Atmos., 114, 1–13, https://doi.org/10.1029/2008JD011671, 2009.